Wafer-Scale AA-Stacked Hexagonal Boron Nitride Grown on GaN Substrate

Seokho Moon[1], Francis Ngome Okello Odongo[1], Adrien Rousseau[2], Chang-Won Choi[1,14], Youngjae Kim[3], Yunjae Park[4], Jiye Kim[1], Jaewon Kim[5], Minhyuk Kim[6], Pierre Valvin[2], Jaehee Cho[7], Kenji Watanabe[8], Takashi Taniguchi[9], Hu Young Jeong[6], Giorgia Fugallo[10], Wilfried Desrat[2], Feng Ding[11,12], Jaedong Lee[3], Bernard Gil[2], Guillaume Cassabois[2,13*], Si-Young Choi[1,14,15*], and Jong Kyu Kim[1,*]

Affiliations:

[1]*Department of Materials Science and Engineering, Pohang University of Science and Technology, Pohang, Republic of Korea*

[2]*Laboratoire Charles Coulomb, UMR5221 CNRS-Universite de Montpellier, Montpellier, France*

[3]*Department of Physics and Chemistry, Daegu Gyeongbuk Institute of Science and Technology (DGIST), Daegu, Republic of Korea*

[4]*Graduate School of Carbon Neutrality, Ulsan National Institute of Science and Technology, Ulsan, Republic of Korea*

[5]*Samsung Advanced Institute of Technology, Suwon, Republic of Korea*

[6]*Graduate School of Semiconductor Materials and Devices Engineering, Ulsan National Institute of Science and Technology, Ulsan, Republic of Korea*

[7]*School of Semiconductor and Chemical Engineering, Jeonbuk National University, Jeonju, Republic of Korea*

[8]*Research Center for Functional Materials, National Institute for Materials Science, 1-1 Namiki, Tsukuba, 305-0044, Japan*

[9]*International Center for Materials Nanoarchitectonics, National Institute for Materials Science, 1-1 Namiki, Tsukuba, 305-0044, Japan*

[10]*LTeN UMR 6607 CNRS-Polytech Nantes, Universite de Nantes, 44306 Nantes, France*

[11]*School of Materials Science and Engineering, Ulsan National Institute of Science and Technology, Ulsan, Republic of Korea*

[12]*Shenzhen Institute of Advanced Technology, Chinese Academy of Science, Shenzhen, China*

[13]*Institut Universitaire de France, 75231 Paris, France*

[14]*Center for Van der Waals Quantum Solids, Institute for Basic Science (IBS), Pohang, Republic of Korea*

[15]*Department of Semiconductor Engineering, Pohang University of Science and Technology, Pohang, Republic of Korea*

*Correspondence to: guillaume.cassabois@umontpellier.fr, youngchoi@postech.ac.kr; kimjk@postech.ac.kr

The stacking sequence of two-dimensional hexagonal boron nitride (h-BN) is a critical factor that determines its polytypes and their distinct physical properties. While most h-BN layers adopt the thermodynamically stable AA' stacking sequence, achieving alternative stacking configurations has remained a long-standing challenge. Here, we demonstrate the scalable synthesis of h-BN featuring unprecedented AA stacking, where atomic monolayers align along the c-axis without any translation or rotation. This previously considered thermodynamically unfavorable h-BN polytype is achieved through epitaxial growth on a 2-inch single crystalline gallium nitride (GaN) wafer, employing a metal-organic chemical vapor deposition (MOCVD) technique. Comprehensive structural and optical characterizations, complemented by theoretical modeling, evidence the formation of AA-stacked multilayer h-BN and reveal that h-BN nucleation on the vicinal GaN surface drives the unidirectional alignment of layers, while electron doping plays a central role in stabilizing the AA stacking configuration. Our findings provide further insights into the scalable synthesis of engineered h-BN polytypes, characterized by unique properties such as large optical nonlinearity.

Two-dimensional (2D) materials are recognized for their extended crystalline planar layered structures, held together by strong covalent in-plane bonds and weak interlayer van der Waals interactions. The stacking sequence of 2D materials plays a pivotal role in determining the interactions between adjacent layers, leading to layer-dependent physical, chemical, and electronic properties. For example, in few-layer graphene, different stacking sequences, such as simple hexagonal (AA), Bernal (AB), and rhombohedral (ABC), induce notable changes in electronic properties, including alterations in the electronic band structure, interlayer screening, and magnetic state[1,2]. Furthermore, by adjusting the twist angles between adjacent layers, intriguing properties emerge with a hexagonal moiré pattern consisting of alternating AA- and AB-stacked regions, including tunable van Hove singularities, anomalous Hall effect, unconventional superconductivity, giving rise to the emerging field of twistronics[3–6].

Hexagonal boron nitride (h-BN) emerges as a promising 2D insulator with a wide

bandgap of ~ 6 eV and high thermal conductivity[7–10]. It has been widely utilized as an ideal substrate, gate dielectric material, passivation layer, and atomic tunneling layer for electronic devices based on 2D materials[11–15]. More recently, it has gained increased attention as an active optical material, demonstrating the potential to generate stable quantum emission in the visible spectral range[16,17]. Additionally, it has shown promise for applications involving deep-ultraviolet (DUV) emitters[18,19] and detectors[20]. This heightened attention towards h-BN as an active optical material can be attributed to its remarkable internal quantum efficiency for band-edge emission, despite the indirect nature of its bandgap[8,21,22]. Unlike graphene, h-BN is composed of two elements, B and N, leading to more stacking types. The electronic and optical properties of multilayer h-BN with stacking types have been explored through theoretical and experimental investigations[23–27]. The two primary stacking sequences extensively explored are AA' and AB configurations. In conventional h-BN bulk crystals, the adjacent monolayers are rotated in a manner where B and N atoms alternate along the c-axis, resulting in the AA' stacking sequence. This configuration restores the inversion symmetry that is broken in the monolayer. When monolayers are stacked without rotation along the c-axis (AA stacking), an in-plane translation can take place, leading to a metastable AB stacking configuration. In the AB stacking configuration, half of the B(N) atoms align with half of the N(B) atoms in the adjacent layers, while the remaining half align with the empty hexagon centers in the adjacent layers. Besides the AA' and AB stacking sequences, there exists a rhombohedral BN structure where each monolayer is successively translated along the $[1\bar{1}00]$ direction by 0.145 nm (ABC stacking)[28]. Despite the potential for the native stacking sequence of bulk crystal to be altered through exfoliation procedures[29], as far as our knowledge extends, no other stacking configurations have been reported for the growth of high-symmetry h-BN polytypes besides AA', AB and ABC.

Here we report the growth of few-layer h-BN featuring an unprecedented AA stacking configuration on a 2-inch single crystalline GaN on sapphire substrate using an MOCVD, as illustrated schematically in Figs. 1a, b (Further details in Methods). Notably, unlike h-BN films grown on conventional substrates such as Cu, Ni, and sapphire, which typically exhibit atomically flat surface[30–34], our h-BN film was synthesized in an unconventional manner. It forms a suspended few-layer film supported by GaN nano-needles, as shown in top- and bird eye-view scanning electron micrographs (Fig. 1c,d, and Supplementary Fig. 1). The chemical properties of the suspended h-BN film were investigated by X-ray photoelectron spectroscopy (XPS) and near-edge X-ray absorption fine structure (NEXAFS) using synchrotron radiation,

and Raman spectroscopy. The XPS survey scan spectrum revealed the presence of B and N elements in the film as well as Ga and N elements in the substrate (Supplementary Fig. 1a). In the NEXAFS spectra shown in Supplementary Fig. 1b, the peaks labeled π* (192.0 eV in the B K-edge and 403.4 eV in the N K-edge) and σ* (198.5 eV in the B K-edge and higher than 408.5 eV in the N K-edge) correspond to the transition of B 1s or N 1s electrons to $2p_{\pi^*}$ and $2p_{\sigma^*}$ states, respectively. These spectra provide evidence that B and N atoms within the suspended film are sp^2-hybridized, maintaining a hexagonal layered structure. Further confirmation of the sp^2-hybridized nature of the suspended h-BN film is provided by the Raman mapping images of the E_{2g} in-plane vibration mode of h-BN near 1,370 cm^{-1} in a 2×2 μm^2 region (Supplementary Fig. 1c) and across 35 different areas of the entire 2-inch wafer (Supplementary Fig. 33). As shown in Supplementary Figs. 1c, d and 33, the h-BN film exhibits a variation in the E_{2g} peak position of less than 0.5 rel.cm^{-1} across the wafer, indicating a negligible strain induced by the suspended structure (see Supplementary Note 5: Strain in suspended h-BN film).

The crystallographic details, including stacking sequence of the suspended h-BN film, were unveiled through using fifth-order aberration-corrected scanning transmission electron microscopy (C_s-corrected STEM, JEOL JEM-ARM200F) operated at an acceleration voltage of 80 kV. Dark field micrographs were acquired by low angle annular dark field (LAADF)-STEM with a low collection angle to visualize atomic Z-contrast from the h-BN film (See Methods). The STEM micrograph in Fig.1e reveals a consistent atomic structure across the suspended h-BN. The Fast Fourier Transform (FFT) from the whole image (inset of Fig. 1e) exhibits only a single set of hexagonal spots, and d-spacings are ~2.07 Å for $(10\bar{1}0)$ and ~1.18 Å for $(11\bar{2}0)$, aligning well with reported values for h-BN[35]. Selected-area electron diffraction (SAED) patterns measured at 53 locations across the 2-inch wafer, shown in Fig. 1f and Supplementary Fig.37c, display single set of hexagonal spots with a consistent d-spacing, indicating uniform growth of h-BN at the wafer scale.

To verify the stacking sequence in the MOCVD-grown h-BN film, we examined the regions encompassing mono-layer (1L), bi-layer (2L), and tri-layer (3L) h-BN in both the grown h-BN film and a h-BN film exfoliated from a single crystal in the AA' stacking sequence, as shown in Figs. 2a,b, respectively. Thanks to its thickness-sensitive Z-characteristic, the number of h-BN layers in the LAADF-STEM micrographs can be precisely identified[36]. Additionally, the atomic number dependence of the LAADF-STEM signal, i.e., Z-contrast,

results in an intensity contrast in the hexagonal lattice forming a distinct geometric configuration. Notably, the brighter spots from the MOCVD-grown h-BN exhibit a triangular configuration regardless of the number of layers, while the exfoliated h-BN shows a hexagonal configuration. This distinction suggests that the MOCVD-grown h-BN possesses a stacking sequence distinct from the exfoliated h-BN having AA' stacking sequence (See also Supplementary Fig.2). Figure 2c shows the simulated LAADF-STEM images along with corresponding schematic atomic configurations of h-BN film containing 1L, 2L, and 3L h-BN with AA and AA' stacking sequences, respectively. The brighter spots in 1L h-BN correspond to the atomic positions of N atoms (Z=7) in the hexagonal lattice, forming a triangular configuration. In the case of 2L and 3L AA-stacked h-BN, triangular configurations are also observed and become brighter as the number of layers increases, due to the accumulation of intensity on the atomic columns of N atoms along the c-axis. On the other hand, the 2L and 3L AA'-stacked h-BN exhibit hexagonal configurations, although the intensity contrast between adjacent atomic columns along the *c*-axis varies with the number of layers.

The LAADF-STEM intensity across a row of atoms within the boxed regions in Figs. 2a,b also exhibits a distinct difference in intensity contrast of adjacent atomic columns between the MOCVD-grown and the exfoliated h-BN film, as shown in Fig. 2d. The relative LAADF-STEM intensity variations across adjacent atomic columns are notably larger for the MOCVD-grown h-BN compared to the exfoliated one. This observation aligns with the Z-contrast signal arising from the accumulation of intensity on the atomic columns along the c-axis of AA-stacked h-BN. Note that the experimental intensity contrasts of adjacent atomic columns match well with the simulated ones with AA and AA' stacking sequences (See also Supplementary Fig. 3). These structural analyses provide strong evidence that the MOCVD-grown suspended h-BN has unprecedented AA stacking sequence. In addition, a convolutional neural network (CNN) model was employed for the identification of the stacking sequence and number of layers in the h-BN film through training, providing compelling evidence that the MOCVD-grown h-BN possesses an unprecedented AA stacking sequence (see Supplementary Fig. 4).

Besides the distinct atomic configurations in in-plane LAADF-STEM images, another crucial structural difference between AA and AA'-stacked h-BN layers is the interlayer distance. The interlayer distance of AA-stacked h-BN is larger than that of AA'-stacked h-BN due to stronger electrostatic repulsion between same atomic species along the c-axis[37]. The cross-sectional annular bright field (ABF)-STEM and high-resolution transmission electron

microscope (HRTEM) micrographs (Fig. 5f, Supplementary Figs. 5, 35 and 36) reveal an average interlayer distance of ~ 0.355 nm, notably larger than that of exfoliated h-BN with AA' stacking sequence (~ 0.33 nm)[38]. This offers additional microstructural evidence that the MOCVD-grown h-BN has an AA stacking sequence (Supplementary Fig. 6)[37,39]. Using a synergistic ensemble of (i) LAADF-STEM imaging, (ii) atomic simulations, (iii) CNN-based analysis, and (iv) cross-sectional ABF-STEM and HRTEM imaging, we have demonstrated that the suspended h-BN film grown by MOCVD possesses an unprecedented AA stacking configuration. Hereafter, we will refer to the h-BN with an AA/AA' stacking as (AA)/(AA') h-BN.

Apart from above nano-structural analyses, (AA)h-BN is characterized by optical spectroscopy with the two-fold objective of identifying the specific signatures of the unusual AA stacking and using them to demonstrate the uniformity of the AA stacking at the wafer level. Key fingerprints are provided by second harmonic generation (SHG), photoluminescence (PL), and second-order resonant Raman scattering, the combination of these techniques illustrating the consequences of the different crystal structure and symmetry between the AA and AA' stackings (Fig.3a).

The first major difference of the AA stacking is the broken inversion symmetry compared to the conventional AA' stacking (Fig.3a). In (AA)h-BN, the simple piling of atomically-thin h-BN layers with neither rotation nor translation retains the symmetry of the h-BN basal plane, which is non-centrosymmetric. SHG is an optical process originating from the $\chi^{(2)}$ nonlinear susceptibility, which is known to be very sensitive to inversion symmetry. SHG was used to discriminate h-BN polytypes either in the AA' stacking, or in the non-centrosymmetric AB one[25]. A large enhancement of SHG was also observed in ultrathin h-BN multilayers in the AA' stacking for odd numbers of h-BN monolayers[9,40]. SHG experiments are performed by illuminating the MOCVD-grown (AA)h-BN film with femtosecond pulses at a wavelength ~ 405 nm in a confocal microscope operating in the UV range (see Methods). Fig.3b displays SHG spectra randomly recorded at various positions across the 2-inch wafer. Intense SHG at half the wavelength of excitation is detected with intensity fluctuations on the order of 10 % (Supplementary Fig. 7) except for isolated hot spots (see Supplementary Fig. 8) that we attribute to the apex of GaN nano-needles beneath the (AA)h-BN film, where a fourteen-fold enhancement of SHG can occur. Excluding these hot spots, SHG in the 2.5 nm-thick MOCVD-grown (AA)h-BN film is typically 2-3 times stronger than in a flake of the same

thickness (Fig.3c), exfoliated from a high-quality bulk (AA')h-BN crystal from NIMS-Japan[41]. Taking into account the influence of the substrate on the electromagnetic field at the excitation wavelength (see details in Supplementary Note «Optical absorption»), we calculate a reduction of the electric field amplitude by a factor ~1.5 from the silicon-on-insulator (SOI) substrate used for the exfoliated 2.5 nm-thick (AA')h-BN to the porous GaN template on which the 2.5 nm-thick (AA)h-BN is grown. After renormalization from the substrate effect following a quadratic dependence of the SHG with the incident power, the SHG signal appears to be 10-15 more intense in (AA)h-BN than in (AA')h-BN. The non-vanishing SHG signal detected in the 2.5 nm-thick (AA')h-BN, although lower than in the MOCVD-grown (AA)h-BN film, may come from an odd number of layers in the exfoliated flake, and from parasitic SHG at the bottom interface of the h-BN flake, which is known to be affected by a thin contamination or water layer between the SiO_2 surface and h-BN [41,42]. In any case, the intense SHG consistently observed over the entire (AA)h-BN wafer is a first definitive signature of the specific symmetry associated with AA stacking.

The second major difference between the AA and AA' stackings lies in their unit cell, which is built from only one atomic layer in (AA)h-BN, instead of two for (AA')h-BN (Fig.3a). With two boron and two nitrogen atoms in the unit cell, (AA')h-BN possesses a Raman-active phonon mode at ~50 cm^{-1} corresponding to the shear rigid motion between adjacent layers. Besides being observable in Raman scattering experiments[43], this shear mode impacts the PL lineshape through a series of overtones at the origin of the slowly-decaying intensity on the low-energy side of the emission lines in (AA')h-BN (Fig.3e)[44]. On the other hand, in (AA)h-BN with only one boron and one nitrogen atoms in the unit cell, this phonon mode no longer exists by symmetry. Since the detection of the low-energy Raman mode is very challenging in few-atomic-layer (AA')h-BN[45], its absence in the low-energy Raman spectrum of (AA)h-BN of nanometric thickness cannot be very conclusive. On the contrary, it is expected to directly impact the profile of the near band-edge luminescence lines. Fig.3d displays a set of PL spectra randomly recorded at the various locations across the 2-inch wafer separated by typical one millimeter, by means of a confocal cryomicroscope operating in the DUV range (see Methods). Albeit minor differences, all spectra consist in an intense component at ~5.77 eV (λ~215 nm) and a weaker one at ~5.84 eV (λ~211 nm), accompanied by a red-shifted satellite lying ~150 meV below in energy. Importantly, all spectra exhibit an abrupt rise of the PL at ~5.74 eV, which is very unusual in h-BN and contrasts with the gradual decay of the PL intensity observed in (AA')h-BN (Fig.3e). Such a difference between (AA) and (AA')h-BN is a direct consequence

of the absence of the interlayer shear mode in (AA)h-BN by symmetry. The steep increase of the PL intensity at ~5.74 eV is reminiscent of the intrinsic line profile of optical transitions in h-BN, hidden in (AA') and (AB)h-BN by the interlayer shear mode overtones[8,44]. Remarkably, the abrupt flank of the PL line is resolved despite the nanometric thickness of the (AA)h-BN film, while the multiplet structure of the interlayer shear mode overtones in (AA')h-BN of the same thickness is largely smeared out compared to the bulk form (Fig.3e). The steep increase of the PL intensity at ~5.74 eV is thus a second specific signature of the AA stacking, that is systematically observed over the whole wafer (Fig.3d and Supplementary Fig.34).

The electronic band structures of (AA)h-BN and (AA')h-BN evaluated in the framework of many-body GW calculations are displayed in Fig.4a. These calculations are performed for an AA stacking with the lattice parameters measured in TEM. The fundamental bandgap is indirect as for (AA')h-BN, with a subtle modification of the conduction band minimum which moves from **M** in the AA' stacking to **L** in the AA stacking (Fig. 4a). Since the valence band maximum is at **K** for both stackings, the minimum of the excitonic dispersion is vertically translated from the **T** to the **S** point of the Brillouin zone from (AA')h-BN to (AA)h-BN (see Brillouin zone in Fig. 4d). Phonon-assisted recombination in indirect-gap (AA)h-BN thus involves phonon modes at the **S** point, instead of **T** for (AA')h-BN. Such an effect changes the electron-phonon matrix elements and explains the modified relative intensity of the optical phonon replicas in (AA) and (AA')h-BN (see Supplementary Note 3.6: Electron-phonon interaction processes in (AA) and (AA')h-BN and Supplementary Fig. 9,10). From the analysis of the phonon-assisted recombination lines and the optical selection rules (see Supplementary Note 3: Band structure of (AA)h-BN), we find that the fundamental indirect exciton lies at an energy of 5.915 eV in (AA)h-BN. This is the lowest excitonic gap of sp^2-bonded BN among the highly-ordered AA', AB and AA stackings (see Supplementary Fig. 11).

Another striking difference between (AA) and (AA')h-BN is the absence of recombination from excitons localized at stacking faults in (AA)h-BN (Fig.3e), a fingerprint related to the broken inversion symmetry in the AA stacking (Fig.3a). Considering the AA' stacking as a reference, polytypes of class (I) can be defined by an in-plane translation of the second basal plane in the unit cell, with limit cases corresponding to AB_1 and AB_2[46] (or A'B and AB' in another convention[39]). Conversely, starting from the AA stacking, an in-plane translation of the second basal plane generates polytypes of class (II), with the AB stacking of Bernal BN as a limit case [39,46]. These two classes differ by a 60°-rotation of every two basal

planes so that one cannot easily transform polytypes from one class to another starting from a crystal in a given stacking. Importantly, all polytypes are centrosymmetric in class (I) but not in class (II). Polytypes of class (I) have excitonic gaps at lower energy than (AA')h-BN [47] so that stacking faults in (AA')h-BN give rise to a PL signal that is redshifted compared to the intrinsic phonon replicas, and that lies below 5.6 eV (shaded area, Fig.3e). On the contrary, in the case of (AA)h-BN, the stacking faults preferentially belong to class (II). Since the (AB)h-BN gap is located at higher energy around ~6.04 eV[25,26], the situation is reversed with respect to (AA')h-BN. The recombination of excitons localized at (AA)h-BN stacking faults would be blue-shifted compared to the bandgap of (AA)h-BN at 5.915 eV. The efficient carrier relaxation to the fundamental excitonic states of the AA stacking prevents any hot luminescence above 5.915 eV, as seen in Fig.3e. In other words, the band-edge emission in (AA)h-BN appears to be protected from the excitonic recombination at extended defects as a result of the peculiar crystal symmetry of the AA stacking.

Moreover, we provide an additional optical signature that differentiates h-BN in the two AA and AA' stackings, and that deals with resonant Raman scattering (Fig.3f). Because the Raman scattering tensor derives from the $\chi^{(3)}$ nonlinear susceptibility, no particular selection rule is expected from the broken inversion symmetry of (AA)h-BN. The effect at stake here is the modification of the resonance conditions for observing the second-order Raman response, resulting from the different electronic band structures of (AA) and (AA')h-BN (Fig.4). By performing Raman scattering experiments with a laser excitation at ~6.4 eV (see Methods), no signal is recorded in the 2.5 nm-thick (AA')h-BN reference sample whereas a complex multiplet at ~2500 cm^{-1} is detected in the MOCVD-grown (AA)h-BN films of the same thickness (Fig.3f), very similar to the second-order Raman scattering spectrum reported in Ref.[48] (black line, Fig.3f). Since the high-energy Raman mode of h-BN has an energy of ~1370 cm^{-1}, wavenumbers around 2,500 cm^{-1} in Fig.3f correspond to second-order Raman scattering processes, involving pairs of phonons of opposite momenta, spanning the full Brillouin zone, hence the similarity of the second-order Raman spectrum with the phonon density of states[48]. The second-order Raman scattering spectrum hardly depends on the stacking sequence or layer number[49] because the phonon density of states is only marginally affected, as is the case in h-BN[25,50]. The second-order Raman scattering spectra of (AA) and (AA')h-BN are thus expected to be very similar. However, their intensity changes here depending on the stacking sequence. The Raman signal is below noise for 2.5 nm-thick (AA')h-BN because of the low efficiency of

this high-order Raman process. The 40 meV red-shift of the bandgap and modified excitonic dispersion in (AA)h-BN provide resonance conditions that enhance the second-order Raman scattering signal above the detection limit, similarly to the phenomenology observed in monolayer h-BN versus multilayer (AA')h-BN[51]. We stress that the detection of second-order resonant Raman scattering in (AA)h-BN is reproducibly obtained over the whole h-BN wafer (Supplementary Fig. 12), further evidencing the scalable growth of h-BN in the AA stacking by our MOCVD technique.

Remarkably, we estimate comparable radiative efficiencies in both (AA) and (AA')h-BN films of 2.5 nm-thickness, thus demonstrating the high-quality of MOCVD-grown (AA)h-BN. As for the flat and parallel bands in the electronic band structure of h-BN in the AA' stacking[22], excitons in (AA)h-BN are built from many independent-particle transitions distributed along high-symmetry directions of the Brillouin zone (Fig. 4b,c). From the solution of the Bethe-Salpeter equation (see Supplementary Note 3.5: Ab initio calculations), the fundamental indirect exciton in (AA)h-BN is the superposition of electron-hole pair states corresponding to occupied conduction states mostly located along **LM** (Fig. 4c) and vacant valence states along **KH** (Fig. 4b). In contrast to transition metal dichalcogenides where the excitonic wavefunction is strongly localized in **K** valleys, excitons in sp^2-bonded BN have a significant extent along high-symmetry directions[52]. This results in optical transitions of high oscillator strength because of the corresponding large joint density of states[22], and it contributes to reaching a high quantum efficiency in our (AA)h-BN sample, of the same order as in high-quality (AA')h-BN crystals from NIMS-Japan.

To investigate the mechanism underlying the formation of the (AA)h-BN, we obtained cross-sectional STEM images at the interface between (AA)h-BN and the GaN substrate during the nucleation stage of h-BN growth (Figs. 5b, c). The atomic force microscopy (AFM) image of the bare GaN substrate reveals an atomic step-terrace topography (Fig. 5a). The facet-dependent anisotropic etching of GaN, especially near dislocations, leads to an increased density of atomic steps. Our series of experiments indicate that H_2 carrier gas plays a pivotal role in the formation of suspended h-BN films on GaN nano-needles via chemical vapor-phase etching of GaN (see Supplementary Note 6: The formation of suspended h-BN film). At elevated growth temperatures, hydrogen atoms introduced to the GaN surface can induce GaN decomposition, particularly initiated at crystalline defects and facets with N-terminated GaN, such as $\{10\bar{1}1\}$, $\{11\bar{2}2\}$[53], resulting in the creation of GaN nano-needle structures. The typical

atomic structures at vicinal or etched surface of Ga-polar GaN (0001) consist of Ga-terminated terrace regions and N-terminated steps. During MOCVD growth under nitrogen-rich conditions with H_2 carrier gas, metal adatoms preferentially incorporate at N-terminated steps, while nitrogen adatoms favor incorporation on the terrace regions due to their lower adsorption energies[54] The adsorption of boron adatoms at the N-terminated steps can be a pivotal factor in determining the stacking sequence of multilayer h-BN. Indeed, h-BN nucleates from the N-terminated step edge of the GaN substrates and grows on the Ga-terminated terrace along the [10-10] direction (Fig. 5c). Our DFT calculations indicate that the coupling between the B-terminated zigzag edge of h-BN and the N-terminated steps of Ga-polar GaN substrates is energetically favored (Figs. 5g, h). This suggests a mechanism of step-edge guided growth with a preferred orientation, whereby h-BN layers nucleating from the vicinal GaN surfaces maintain the same orientation, resulting in a zero-twisting angle between neighboring layers. This process includes the formation of (AA)h-BN or (AB)h-BN, while eliminating the possibility of forming (AA')h-BN, which requires a 60-degree rotation of adjacent h-BN layers. Our investigation provided clear nano-structural and optical evidence exclusively for (AA)h-BN across the 2-inch wafer. This was demonstrated through both top-view (Fig. 2 and Supplementary Figs.2,3,38) and cross-sectional STEM images (Fig. 5 and Supplementary Figs. 5, 35, 36), as well as PL measurements (Fig. 3 and Supplementary Fig.13). No evidence of (AB)h-BN was observed in our study.

It is important to note that large area (AA)h-BN cannot exist for a long time unless it is more stable than h-BN with other possible stacking orders. Our DFT calculations further reveal that the formation of the AA stacking sequence in h-BN can be energetically more favorable than the AB and AA' stacking sequence when the electron density within h-BN layers exceeds a certain threshold (Supplementary Fig. 21a), which can be influenced by factors such as the incorporation of carbon during MOCVD growth. Since carbon-containing TEB[(CH3CH2)3B] is used as B precursor, carbon atoms can be incorporated into the h-BN layers from the very initial stages of the growth. Indeed, small amounts of carbon in h-BN layers were detected even when grown for a short duration (5 pulsed cycles, approximately 1 minute) (Supplementary Figs. 22 and 23). The incorporated carbon substitutes at boron sites (C_B) (Supplementary Fig. 38), introducing excess electrons into h-BN layers (Supplementary Figs. 24 and 25). Because of the ionic character of the intralayer bonding in h-BN layer, the valence-band maximum is primarily derived from π-states associated with nitrogen $2p_z$ orbitals and the conduction-band minimum is mainly derived from π^*- states involving boron

empty $2p_z$ orbitals[7,55]. Consequently, the excess electrons occupy the out-of-plane boron $2p_z$ orbitals of h-BN layers, significantly influencing interlayer interactions, thus the stacking sequence of these layers (Supplementary Fig.21b). In the case of (AB)h-BN or (AA')h-BN, where boron and nitrogen atoms are alternately eclipsed within the same atomic columns, excess electrons occupying the out-of-plane boron $2p_z$ orbitals of h-BN layers lead to structural instability due to increased repulsive Pauli interactions with electrons occupying the out-of-plane nitrogen $2p_z$ orbitals of adjacent layers. On the other hand, the excess electrons in (AA)h-BN contribute to structural stability due to the absence of repulsive Pauli interactions with the empty boron $2p_z$ orbitals of adjacent layers (see Supplementary Note 4: Stability of h-BN polytypes with injected electrons). Under this growth mechanism, the nucleation of (AA)h-BN occurs at the neighboring step edges of GaN substrates (Supplementary Fig.27), and subsequently, the (AA)h-BN film grows on the GaN substrate, aligned along the c-axis after coalescence. (Fig.5d and e).

In conclusion, we report the synthesis of unprecedented AA-stacked h-BN on a 2-inch GaN wafer using MOCVD. The MOCVD-grown h-BN films consist of ~ 7 atomic monolayers stacked in the AA configuration, which are suspended on GaN nano-needles. Using a synergistic ensemble of microstructural analyses including LAADF-STEM imaging, atomic simulations, CNN-based analysis, and cross-sectional ABF-STEM imaging, we have demonstrated that the suspended h-BN film grown by MOCVD possesses AA stacking configuration. Furthermore, the SHG, second-order Raman, and DUV PL spectra reveal at least five distinctive optical characteristics that exclusively manifest through the h-BN with AA stacking. Surprisingly, the internal quantum efficiency of the (AA)h-BN is estimated to be comparable to that of the (AA')h-BN exfoliated from high-quality bulk crystals, despite its intrinsic indirect bandgap nature, due to the high crystal quality and the unique optical property of the (AA)h-BN protected from stacking faults-related radiative recombination. These findings offer a great potential of (AA)h-BN for dimensionally-thin-yet-optically-thick DUV optoelectronics. We proposed a step-edge guided growth mechanism with a preferred orientation, wherein h-BN nucleates from the N-terminated step edge of vicinal GaN substrates and grows unidirectionally across the Ga-terminated terrace, while electron doping contributes to stabilizing the AA stacking configuration. We firmly believe that our findings expand the understanding of the scalable synthesis methods for multilayer h-BN with engineered polytypes and present an opportunity to explore unique properties arising from its

unprecedented crystal structures. These advancements have practical implementations on various fields including efficient DUV optoelectronics, potential ultrathin quantum photonic and ferroelectric applications by utilizing large optical nonlinearity and superior ferroelectricity compared to the (AA')h-BN.

Acknowledgements: This work was supported by National Research Foundation of Korea (NRF) grant funded by the Korean Government (MSIT) (NRF-2018H1A2A1060392, NRF-2018-Global Ph.D. Fellowship Program, NRF-2021M3C1C3097673, RS-2022-NR068223, RS-2024-00344690, and RS-2024-00355591), the Technology Innovation Program (Grant No. 20016290, development of sub-micrometer blue color light source for modular display) funded by the Ministry of Trade, Industry & Energy (MOTIE, Korea). S.M., Jiye Kim, Jaewon Kim, and J.K.K. are grateful for the financial support of Samsung Electronics Co.,Ltd (IO201215-08185-01) and Samsung Funding & Incubation Center of Samsung Electronics under Project Number SRFC-MA1401-10. S.M. and J.K.K. acknowledge support by internal fund/grant of Electronics and Telecommunications Research Institute (ETRI) (25YH1100, Development of nano-sheet transfer-based ultra-thin GaN transistor technology). A.R., P.V., B.G., and G.C. are grateful for financial support by the BONASPES (ANR-19-CE30-0007), ZEOLIGHT (ANR-19-CE08-0016) and HETEROBNC (ANR-20-CE09-0014-02) projects. F.N.O.O., C.-W.C, and S.-Y.C. acknowledge support by Korea Basic Science Institute (National research Facilities and Equipment Center) grant funded by the Ministry of Education (2020R1A6C101A202). We are grateful to Keun Su Kim at Yonsei University, Republic of Korea, for helpful discussions on the investigations of the band structure of h-BN polytypes.

Author contributions:

S.M. and J.K.K. conceived the study. G.C., S.-Y.C., and J.K.K. supervised the project. S.M. conducted the growth of AA-stacked h-BN films. S.M., F.N.O.O., and C.-W.C. organized the structural characterization. A.R., P.V., B.G., and G.C. performed the PL, SHG, reflectivity, and second-order Raman scattering measurements. Y.K., G.F., W.D., and J.L. carried out the theoretical calculations of optical properties. S.M., Y.P., F.D., and J.K.K. developed the growth mechanism. S.M., Jiye Kim, Jaewon Kim, and J.C. prepared GaN substrates. K.W. and T.T. provided the h-BN crystals. S.M., C.-W.C., M.K., and H.Y.J. prepared samples for STEM and

TEM measurements. S.M. carried out the SEM, AFM, Raman, XPS, NEXAFS and UPS measurements. All authors contributed to the writing of the manuscript.

Competing interests:

The authors declare no competing interests.

Figure Captions:

Figure 1 | MOCVD-grown suspended h-BN film on GaN nano-needles. a, Schematic illustration of the h-BN film on GaN nano-needles grown by MOCVD. **b**, Photograph of as-grown 2-inch h-BN film on a GaN/sapphire wafer. **c,d,** top (**c**) and tilted (**d**) view false-color SEM images. **e,** Atomic-resolution LAADF-STEM image of MOCVD grown h-BN. The inset FFT spots reveal typical h-BN six-fold symmetry composed of $(10\bar{1}0)$ and $(11\bar{2}0)$ reflections. Scale bars, 0.5 nm. **f**, Four SAED patterns recorded at different locations across the 2-inch wafer labeled in **b**.

Figure 2 | Structural investigation of MOCVD grown suspended (AA)h-BN on GaN nano-needles. a,b, LAADF-STEM images of MOCVD grown suspended (AA)h-BN (**a**) and conventionally exfoliated (AA')h-BN from high-quality bulk crystal (**b**). Mono-, bi- and tri-layer regions are marked as 1L, 2L, and 3L, respectively. Scale bars, 0.5 nm. The typical bi- and tri-layer regions of (AA)h-BN and (AA')h-BN exhibiting triangular and hexagonal configuration of the brighter spots are shown in the lower panel. The corresponding atomic model with nitrogen/boron atoms indicated by ivory/light navy solid balls is shown for clarity. **c,** Simulated LAADF-STEM images of mono-, bi- and tri-layer (AA)h-BN and (AA')h-BN showing thickness-dependent contrast variation. **d**, The experimental LAADF-STEM intensity profiles of mono-, bi- and tri-layer (AA)h-BN (red) and (AA')h-BN (blue) extracted from the boxed regions marked in **a** and **b**. The red and blue arrows designate the brighter spots in **a** and **b**.

Figure 3 | Optical properties of (AA) and (AA')h-BN films. a, Schematic illustration of the crystal structure of (AA)h-BN and (AA')h-BN. **b**, SHG spectra of (AA)h-BN at 25 different areas across the entire 2-inch wafer under excitation at 405 nm. Inset: schematic illustration of the SHG response of (AA)h-BN. **c**, Comparison of the SHG spectra of two h-BN films of the same thickness (2.5 nm) but in different stacking: AA (red line), and AA' (blue line). **d**, Photoluminescence of (AA)h-BN at 25 different areas along a 2-inch wafer measured in the DUV at cryogenic temperature (T=6K). **e**, Comparison of the PL spectra of three h-BN samples: 2.5 nm-thick (AA)h-BN (top curve, red line), 2.5 nm-thick (AA')h-BN (middle curve, blue line), and (AA')h-BN bulk crystal (bottom curve, black). The abrupt rise of the

460 photoluminescence signal at 5.74 eV in (AA)h-BN contrasts with the smooth decrease in
461 (AA')h-BN, and it is the fingerprint for the absence of the interlayer shear mode in the AA
462 stacking. Extended defects emission is indicated by the shaded areas, and it is red-shifted with
463 respect to the bandgap in (AA')h-BN, but blue-shifted in the case of (AA)h-BN. **f**, Second-
464 order Raman scattering in h-BN measured from 2.5 nm-thick (AA)h-BN (red line) and 2.5 nm-
465 thick (AA')h-BN (blue line). The black line is the experimental spectrum measured by Reich
466 *et al*.[48]
467

468 **Figure 4 | Calculated electronic band structure of (AA) and (AA')h-BN and color map of**
469 **weighted oscillator strengths building the fundamental indirect exciton. a**, Electronic band
470 structure evaluated in the framework of many-body GW calculations for AA' structure and AA
471 structure. Orange arrows indicate the indirect band-gap along **K**-**M** for the AA' and **K**-**L** for
472 the AA structure as discussed in the text. **b**,**c**, Color maps in the Brillouin zone of the weighted
473 oscillator strengths $A_{\lambda}^{t}\rho^{t}$ (see Supplementary Note 3.5: Ab initio calculations) building the
474 fundamental indirect exciton at **q**=**S.** This exciton is the superposition of electron-hole pair
475 states corresponding to vacant valence states along **KH** (**b**) and occupied conduction states
476 along **LM** (**c**). For the sake of clarity, the map is limited to the points of the prevailing direct
477 independent-particle transitions that contribute in total to 80% of the exciton absorption. The
478 irreducible part of the Brillouin zone is delimited by red lines, which are thicker for the **KH** (**b**)
479 and **ML** (**c**) paths. **d**, The irreducible part of the Brillouin zone.
480

481 **Figure 5 | The growth mechanism of (AA)h-BN. a,** schematic of the step-edge guided growth
482 of (AA)h-BN from the vicinal GaN surfaces**.** Inset, Surface morphology of bare GaN substrates
483 measured by AFM. **b,c,** Structural investigation of the nucleation of the (AA)h-BN from the
484 step edge of GaN substrate. LAADF (green)- and contrast-inverted ABF (red)- STEM
485 micrographs are overlaid to clearly identify the location of each atom. Low-magnification (**b**)
486 and high-magnification (**c**) STEM micrographs obtained from an overlay in Supplementary
487 Fig.39b with schematics of atomics structure of h-BN and GaN. **d**, cross-sectional color-mixed
488 STEM image of coalesced (AA)h-BN on the terrace of GaN substrate, and the corresponding
489 FFT image (**e**). **f**, experimental and simulated cross-sectional ABF-STEM images of suspended
490 (AA)h-BN. A comparison of intensity profiles between simulated AA-stacked (red line), AA'-
491 stacked (blue line) h-BN with experimental suspended h-BN (black line). **g**, Schematics of the

configuration of h-BN nucleated from the step edge of vicinal GaN surfaces. **h**, The binding energy (E_{bind}) between h-BN and the step edge of GaN depends on termination of h-BN.

References:

1. Mak, K. F., Shan, J. & Heinz, T. F. Electronic Structure of Few-Layer Graphene: Experimental Demonstration of Strong Dependence on Stacking Sequence. *Phys. Rev. Lett.* **104**, 176404 (2010).
2. Bao, C. *et al.* Stacking-Dependent Electronic Structure of Trilayer Graphene Resolved by Nanospot Angle-Resolved Photoemission Spectroscopy. *Nano Lett.* **17**, 1564–1568 (2017).
3. Li, G. *et al.* Observation of Van Hove singularities in twisted graphene layers. *Nature Phys* **6**, 109–113 (2010).
4. Serlin, M. *et al.* Intrinsic quantized anomalous Hall effect in a moiré heterostructure. *Science* **367**, 900–903 (2020).
5. Park, J. M., Cao, Y., Watanabe, K., Taniguchi, T. & Jarillo-Herrero, P. Tunable strongly coupled superconductivity in magic-angle twisted trilayer graphene. *Nature* **590**, 249–255 (2021).
6. Liu, C. *et al.* Designed growth of large bilayer graphene with arbitrary twist angles. *Nat. Mater.* **21**, 1263–1268 (2022).
7. Gilbert, S. M. *et al.* Alternative stacking sequences in hexagonal boron nitride. *2D Mater.* **6**, 021006 (2019).
8. Cassabois, G., Valvin, P. & Gil, B. Hexagonal boron nitride is an indirect bandgap semiconductor. *Nature Photon* **10**, 262–266 (2016).
9. Caldwell, J. D. *et al.* Photonics with hexagonal boron nitride. *Nat Rev Mater* **4**, 552–567 (2019).
10. Moon, S. *et al.* Hexagonal Boron Nitride for Next-Generation Photonics and Electronics. *Advanced Materials* **35**, 2204161 (2023).
11. Lee, G.-H. *et al.* Flexible and Transparent MoS2 Field-Effect Transistors on Hexagonal Boron Nitride-Graphene Heterostructures. *ACS Nano* **7**, 7931–7936 (2013).
12. Dean, C. R. *et al.* Boron nitride substrates for high-quality graphene electronics. *Nature Nanotech* **5**, 722–726 (2010).
13. Britnell, L. *et al.* Field-Effect Tunneling Transistor Based on Vertical Graphene Heterostructures. *Science* **335**, 947–950 (2012).
14. Doganov, R. A. *et al.* Transport properties of pristine few-layer black phosphorus by van der Waals passivation in an inert atmosphere. *Nat Commun* **6**, 6647 (2015).
15. Moon, S. *et al.* Van der Waals Heterostructure of Hexagonal Boron Nitride with an AlGaN/GaN Epitaxial Wafer for High-Performance Radio Frequency Applications. *ACS Appl. Mater. Interfaces* **13**, 59440–59449 (2021).
16. Tran, T. T., Bray, K., Ford, M. J., Toth, M. & Aharonovich, I. Quantum emission from hexagonal boron nitride

monolayers. *Nature Nanotech* **11**, 37–41 (2016).

17. Gottscholl, A. *et al.* Initialization and read-out of intrinsic spin defects in a van der Waals crystal at room temperature. *Nat. Mater.* **19**, 540–545 (2020).
18. Watanabe, K., Taniguchi, T., Niiyama, T., Miya, K. & Taniguchi, M. Far-ultraviolet plane-emission handheld device based on hexagonal boron nitride. *Nature Photon* **3**, 591–594 (2009).
19. Song, S.-B. *et al.* Deep-ultraviolet electroluminescence and photocurrent generation in graphene/hBN/graphene heterostructures. *Nat Commun* **12**, 7134 (2021).
20. Lin, C.-H. *et al.* A flexible solar-blind 2D boron nitride nanopaper-based photodetector with high thermal resistance. *npj 2D Mater Appl* **2**, 1–6 (2018).
21. Schué, L. *et al.* Bright Luminescence from Indirect and Strongly Bound Excitons in h-BN. *Phys. Rev. Lett.* **122**, 067401 (2019).
22. Elias, C. *et al.* Flat Bands and Giant Light-Matter Interaction in Hexagonal Boron Nitride. *Phys. Rev. Lett.* **127**, 137401 (2021).
23. Yasuda, K., Wang, X., Watanabe, K., Taniguchi, T. & Jarillo-Herrero, P. Stacking-engineered ferroelectricity in bilayer boron nitride. *Science* **372**, 1458–1462 (2021).
24. Yao, K. *et al.* Enhanced tunable second harmonic generation from twistable interfaces and vertical superlattices in boron nitride homostructures. *Science Advances* **7**, eabe8691 (2021).
25. Rousseau, A. *et al.* Bernal Boron Nitride Crystals Identified by Deep-Ultraviolet Cryomicroscopy. *ACS Nano* **16**, 2756–2761 (2022).
26. Rousseau, A. *et al.* Determination of the optical bandgap of the Bernal and rhombohedral boron nitride polymorphs. *Phys. Rev. Materials* **5**, 064602 (2021).
27. Gigliotti, J. *et al.* Highly Ordered Boron Nitride/Epigraphene Epitaxial Films on Silicon Carbide by Lateral Epitaxial Deposition. *ACS Nano* **14**, 12962–12971 (2020).
28. Wang, L. *et al.* Bevel-edge epitaxy of ferroelectric rhombohedral boron nitride single crystal. *Nature* **629**, 74–79 (2024).
29. Zribi, J. *et al.* Structural and electronic transitions in few layers of isotopically pure hexagonal boron nitride. *Phys. Rev. B* **102**, 115141 (2020).
30. Wang, L. *et al.* Epitaxial growth of a 100-square-centimetre single-crystal hexagonal boron nitride monolayer on copper. *Nature* **570**, 91–95 (2019).
31. Chen, T.-A. *et al.* Wafer-scale single-crystal hexagonal boron nitride monolayers on Cu (111). *Nature* **579**,

555 219–223 (2020).
556 32. Ma, K. Y. *et al.* Epitaxial single-crystal hexagonal boron nitride multilayers on Ni (111). *Nature* **606**, 88–93
557 (2022).
558 33. Li, X. *et al.* Large-Area Two-Dimensional Layered Hexagonal Boron Nitride Grown on Sapphire by
559 Metalorganic Vapor Phase Epitaxy. *Crystal Growth & Design* **16**, 3409–3415 (2016).
560 34. Jeong, H. *et al.* Wafer-scale and selective-area growth of high-quality hexagonal boron nitride on Ni(111) by
561 metal-organic chemical vapor deposition. *Sci Rep* **9**, 5736 (2019).
562 35. Lee, J. S. *et al.* Wafer-scale single-crystal hexagonal boron nitride film via self-collimated grain formation.
563 *Science* **362**, 817–821 (2018).
564 36. Ngome Okello, O. F., Yang, D.-H., Chu, Y.-S., Yang, S. & Choi, S.-Y. Atomic-level defect modulation and
565 characterization methods in 2D materials. *APL Materials* **9**, 100902 (2021).
566 37. Liu, L., Feng, Y. P. & Shen, Z. X. Structural and electronic properties of h-BN. *Phys. Rev. B* **68**, 104102 (2003).
567 38. Kim, S. M. *et al.* Synthesis of large-area multilayer hexagonal boron nitride for high material performance.
568 *Nat Commun* **6**, 8662 (2015).
569 39. Constantinescu, G., Kuc, A. & Heine, T. Stacking in Bulk and Bilayer Hexagonal Boron Nitride. *Phys. Rev.*
570 *Lett.* **111**, 036104 (2013).
571 40. Li, Y. *et al.* Probing Symmetry Properties of Few-Layer MoS2 and h-BN by Optical Second-Harmonic
572 Generation. *Nano Lett.* **13**, 3329–3333 (2013).
573 41. Rousseau, A. *et al.* Monolayer Boron Nitride: Hyperspectral Imaging in the Deep Ultraviolet. *Nano Lett.* **21**,
574 10133–10138 (2021).
575 42. Gorbachev, R. V. *et al.* Hunting for Monolayer Boron Nitride: Optical and Raman Signatures. *Small* **7**, 465–
576 468 (2011).
577 43. Kuzuba, T., Era, K., Ishii, T. & Sato, T. A low frequency Raman-active vibration of hexagonal boron nitride.
578 *Solid State Communications* **25**, 863–865 (1978).
579 44. Vuong, T. Q. P. *et al.* Overtones of interlayer shear modes in the phonon-assisted emission spectrum of
580 hexagonal boron nitride. *Phys. Rev. B* **95**, 045207 (2017).
581 45. Stenger, I. *et al.* Low frequency Raman spectroscopy of few-atomic-layer thick hBN crystals. *2D Mater.* **4**,
582 031003 (2017).
583 46. Gil, B. *et al.* Polytypes of sp2-Bonded Boron Nitride. *Crystals* **12**, 782 (2022).
584 47. Bourrellier, R. *et al.* Nanometric Resolved Luminescence in h-BN Flakes: Excitons and Stacking Order. *ACS*

Photonics **1**, 857–862 (2014).

48. Reich, S. *et al.* Resonant Raman scattering in cubic and hexagonal boron nitride. *Phys. Rev. B* **71**, 205201 (2005).

49. Qian, Q., Zhang, Z. & Chen, K. J. Layer-dependent second-order Raman intensity of $\mathrm{Mo}{\mathrm{S}}_{2}$ and $\mathrm{WS}{\mathrm{e}}_{2}$: Influence of intervalley scattering. *Phys. Rev. B* **97**, 165409 (2018).

50. Michel, K. H. & Verberck, B. Phonon dispersions and piezoelectricity in bulk and multilayers of hexagonal boron nitride. *Phys. Rev. B* **83**, 115328 (2011).

51. Rousseau, A. *et al.* Spatially-resolved UV-C emission in epitaxial monolayer boron nitride. *2D Mater.* **11**, 025026 (2024).

52. Zhang, F. *et al.* Intervalley Excitonic Hybridization, Optical Selection Rules, and Imperfect Circular Dichroism in Monolayer h-BN. *Phys. Rev. Lett.* **128**, 047402 (2022).

53. Sheng, S. *et al.* Atomic-Scale Investigation of the Lattice-Asymmetry-Driven Anisotropic Sublimation in GaN. *Advanced Science* **9**, 2106028 (2022).

54. Ohka, T., Akiyama, T., Pradipto, A. M., Nakamura, K. & Ito, T. Effect of Step Edges on Adsorption Behavior for GaN(0001) Surfaces during Metalorganic Vapor Phase Epitaxy: An Ab Initio Study. *Crystal Growth & Design* **20**, 4358–4365 (2020).

55. Weston, L., Wickramaratne, D., Mackoit, M., Alkauskas, A. & Van de Walle, C. G. Native point defects and impurities in hexagonal boron nitride. *Phys. Rev. B* **97**, 214104 (2018).

56. Barthel, J. Dr. Probe: A software for high-resolution STEM image simulation. *Ultramicroscopy* **193**, 1–11 (2018).

57. Momma, K. & Izumi, F. VESTA 3 for three-dimensional visualization of crystal, volumetric and morphology data. *J Appl Cryst* **44**, 1272–1276 (2011).

58. Valvin, P. *et al.* Deep ultraviolet hyperspectral cryomicroscopy in boron nitride: Photoluminescence in crystals with an ultra-low defect density. *AIP Advances* **10**, 075025 (2020).

Methods:

MOCVD Growth of h-BN on GaN wafer: The GaN epitaxial structure employed in this work was grown on *c*-plane sapphire by a multiwafer MOCVD system (Aixtron G3) capable of processing 11 × 2-inch wafers simultaneously. Trimethylgallium (TMGa) and ammonia (NH_3) served as the sources for gallium and nitrogen, respectively. The Gan buffer layer was grown at 550 ºC under a reactor pressure of 400 mbar, with NH_3 and TMGa flow rates maintained at 5000 and 30 sccm, respectively. Subsequently, the first high temperature undoped GaN (u-GaN) layer was grown at 1040 ºC and 400 mbar, using NH_3 (5000 sccm) and TMGa (60 sccm) for a duration of 5 minutes. For the second u-GaN layer, the temperature was increased to 1050 ºC, while NH_3 and TMGa flow rates were raised to 8000 and 100 sccm, respectively, over a 5 min period. The growth process then continued for an additional 15 minutes after stabilization. Finally, an n-type doped GaN top layer was subsequently grown at 1050 ºC with NH_3 and TMGa flows of 8000 and 100 sccm, respectively.

The h-BN films were grown on epitaxial GaN wafer using the same MOCVD system utilized for GaN growth, with a reactor temperature of 1050 ºC under reactor pressures from 30 to 600 mbar and H_2 or N_2 carrier gases. To mitigate undesirable parasitic reactions in the gas phase, a pulsed source-injection mode was employed. Each pulse cycle consisted of four steps: (1) TEB injection for 2-5 seconds, (2) a first interruption, where any injection of precursors are paused, for 1-2 seconds , (3) NH_3 injection for 1-4 seconds , and (4) a second interruption for 1-2 seconds. The number of pulse cycles ranged from 5 to 200. The flow rates of TEB and NH_3 were set between 10-21 μmol/min and 8000-16000 sccm, respectively, resulting in a V/III ratio of approximately 13,700-27,400, considering the injection durations. Either H_2 or N_2 was used as a carrier gas, and the total gas flow in the reactor was kept constant throughout the h-BN growth process.

Characterization of h-BN film: Raman spectroscopy was conducted using a commercially available confocal micro-Raman spectrometer (Alpha 300R from WITec). The measurements employed either a 488 nm Ar^+ laser or a 532 nm Nd:YAG laser, with a 1800 lines/mm grating.

To analyze the chemical states of the epitaxially grown h-BN, XPS and NEXAFS spectra were collected at the 4D and 10D soft X-ray beamlines at Pohang Accelerator Laboratory (PAL) in South Korea. For the XPS survey scan, an incident X-ray energy of 650 eV was used, while photon energies of 250 eV and 500 eV were applied for B 1s and N 1s core-level spectra,

642 respectively. NEXAFS data were acquired by tilting the samples at various angles relative to
643 the beam, using partial electron yield (PEY) or total electron yield (TEY) detection methods.

644 The energy band structure was analyzed with UPS on a Nexsa XPS system (ThermoFisher
645 Scientific, UK) at the Korea Basic Science Institute (KBSI). A gas discharge lamp emitting He
646 I radiation (hv=21.2 eV) served as the light source for the UPS measurements.

647 **Transfer of h-BN films**: The as-grown h-BN films were detached from the GaN substrates
648 using a mechanical delamination method. Polymethyl methacrylate (PMMA, 495 K, 8% in
649 anisole) was spin-coated onto the as-grown h-BN film at 2000 rpm for 1 minute, followed by
650 baking at 180 ºC for another minute. A thermal release tape (TRT) was then applied to the
651 PMMA surface as a support layer, and the TRT/PMMA/h-BN stack was mechanically peeled
652 off from the GaN substrate. The detached film was transferred onto a target substrate, and the
653 TRT was removed by heating the assembly at 120 ºC on a hot plate. The PMMA film was
654 subsequently dissolved by immersing the sample in acetone for several hours, leaving the h-
655 BN film on the desired substrate. For STEM analysis, the films were transferred onto Quantifoil
656 holey carbon 200-mesh TEM gold grids and vacuum annealed at 150ºC to eliminate residual
657 contaminants.

658 **Atomic scale imaging and simulations:** The crystal structure of the suspended h-BN films
659 was examined using high-resolution scanning transmission electron microscopy (HR-STEM)
660 with a probe-corrected STEM (ARM-200F, JEOL) equipped with a fifth-order Cs-corrector
661 (ASCOR, CEOS GmbH, Germany). These analyses were conducted at the Materials Imaging
662 and Analysis Center of POSTECH under an accelerating voltage of 80 kV. Low-angle annular
663 dark-field (LAADF) images were obtained with a camera length of 20 cm corresponding to
664 inner and outer detector angles of approximately 23 mrad and 91 mrad, respectively. The probe
665 size was adjusted to 9C, resulting in a current density of ~ 4.5 pA/cm, with a condenser lens
666 aperture of 40 μm. Atomic structure modeling and simulations were performed using Dr.
667 Probe[56] and VESTA[57] software.

668 **Deep-ultraviolet (DUV) spectroscopy:** DUV spectroscopy is performed with the setup
669 described in Ref.[58]. For photoluminescence (PL) measurements, the excitation is provided by
670 the fourth harmonic of a cw mode-locked Ti:Sa oscillator and it is tunable from 193 to 205 nm
671 with trains of 140 fs pulses at 80 MHz repetition rate. For second harmonic generation (SHG),
672 we use the second harmonic of the Ti:Sa oscillator at wavelengths around 400 nm. The injection

path uses a series of dielectric mirrors coated for the spectral ranges of either the second or the fourth harmonic of the laser. The exciting laser beam is focused by a Schwarzschild objective located inside the closed-cycle cryostat equipped with CaF_2 optical windows. The objective numerical aperture is 0.5, resulting in a laser spot size of 200 nm for PL and 400 nm for SHG experiments. The sample is mounted on a stack of piezoelectric steppers and scanners that is cooled down to 6 K under ultrahigh vacuum (10^{-11} bar). The photoluminescence is collected by means of an achromatic optical system comprising a pinhole for confocal filtering. It is then dispersed in a Czerny-Turner spectrometer with 500 mm focal length and a 1200 grooves/mm ruled grating and finally detected by a back-illuminated CCD camera with 13.5 μm pixel size. The corresponding spectral resolution is 0.17 nm (3.3 meV) in PL. The whole setup is controlled by homemade Python modules inserted inside the QUDI software suite to create hyperspectral images of the emitted signal recorded at each point of a scanned area. The PL data displayed in Fig.3 are recorded at 6 K, for an incident power of ~20 μW at an excitation wavelength of 195 nm.

DFT calculation of electron-phonon interaction: We employed the first-principles density functional theory (DFT) implemented in the Quantum espresso v6.1.0 code[59]. In the calculation, the generalised gradient approximation (GGA) of Perdew-Burke-Ernzerhof exchange correlation functional[60] and the wavefunction (density) cutoff of 150 Ry (900 Ry) are adopted with grimme-D2 van der Waals correction. For the calculation of electron-phonon matrix elements implemented in the code, $18 \times 18 \times 10$ and $18 \times 18 \times 6$ **k**-point grids are considered for (AA)h-BN and h-BN, respectively. The matrix elements $g_{mn,\nu}(k,q)$ originally read,

$$g_{mn,\nu}(k,q) = \frac{1}{\sqrt{2\omega_{q\nu}}} \langle \psi_{mk+q}(r) | \partial_{q\nu} V^{scf} | \psi_{nk}(r) \rangle$$

where the phonon of mode ν with momentum q couples between ψ_m and ψ_n of Kohn-Sham eigen statres.

Stability of h-BNs with injected electrons and projected density of states using DFT calculations: We compared the stability of AA, AB, and AA′-stacking types with the hexagonal lattice with the bulk system including 64 atoms in bilayer using the DFT calculations implemented in the Vienna ab initio Simulation Package (VASP)[60–62]. We performed the DFT calculations PBE and GGA[60–62]. Also, grimme-D3 van der Waals correction for the dispersive interactions was adopted[63,64]. The plane-wave cut-off was set to 600 eV with the convergence criterion for the self-consistent field iterations set to 10^{-6} eV. Vacuum slabs with more than 15

Å was used. The Brillouin zone was sampled with a k-points density with less than 0.03 $Å^{-1}$ for the energy calculations. 18×18×4 k-points grid are considered for calculations of the projected density of states for the bulk system including 4 atoms in bilayer using HSE calculations.[65] We performed optimization of the lattice cell and atomic positions until the convergences of the forces on all atoms less than 0.01 eV/Å.

GW Electronic band structure: We performed both G_0W_0 calculation and self-consistent GW (sc-GW) in a 12x12x4 Γ-centered k-point grid to obtain the corrections to the DFT eigenvalues, which were used in a linear interpolation to calculate quasiparticles energies in the whole BZ. The screened Coulomb interaction W, evaluated within the random phase approximation (RPA), converged with 600 bands and a 20 Hartree cutoff. The GW calculations included 640 bands in the plasmon pole approximation. The sc-GW calculations reached the convergence (within 10 meV) after 4 iterations. The GW band structure of the (AA')h-BN reported as reference in Fig. 4a of the main text has been evaluated with the parameters we already reported in Ref. [66]. For a comparison among the band structures obtained with the different theoretical approaches see Supplementary Fig.17.

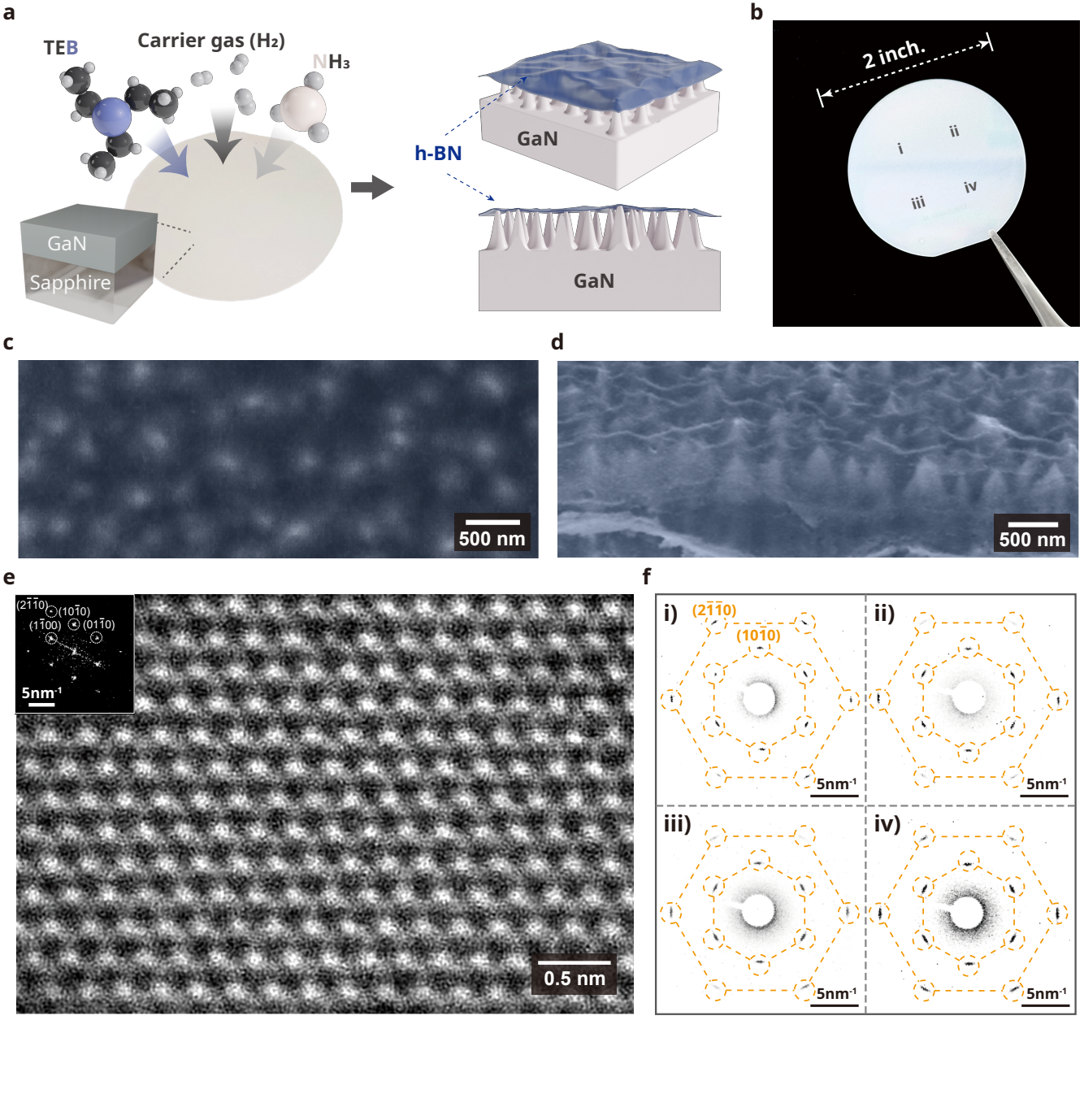
Data Availability:

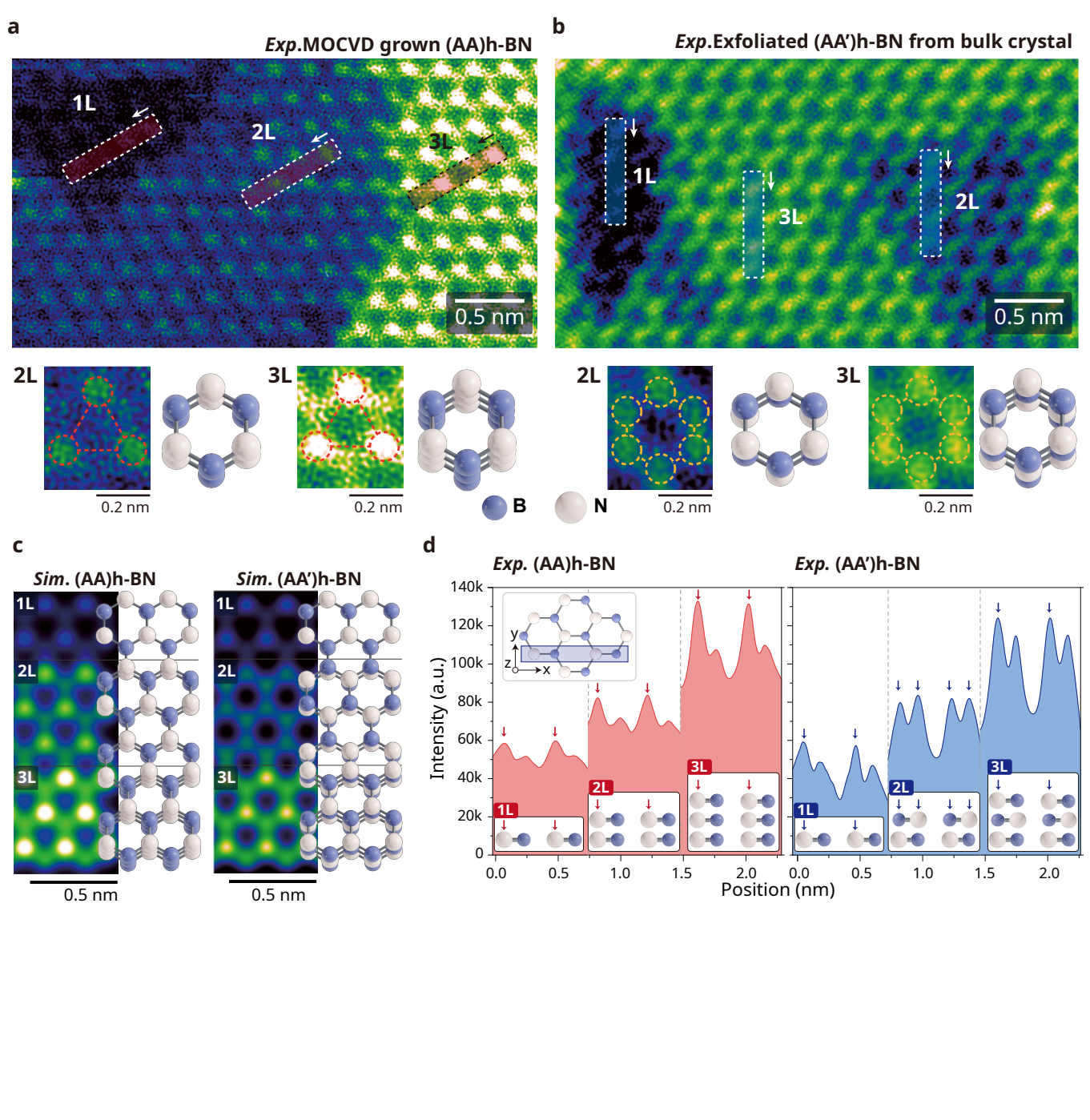
The authors declare that the data supporting the findings of this study are available within the paper and its supplementary information files. Additional data are available from the corresponding authors upon reasonable request.

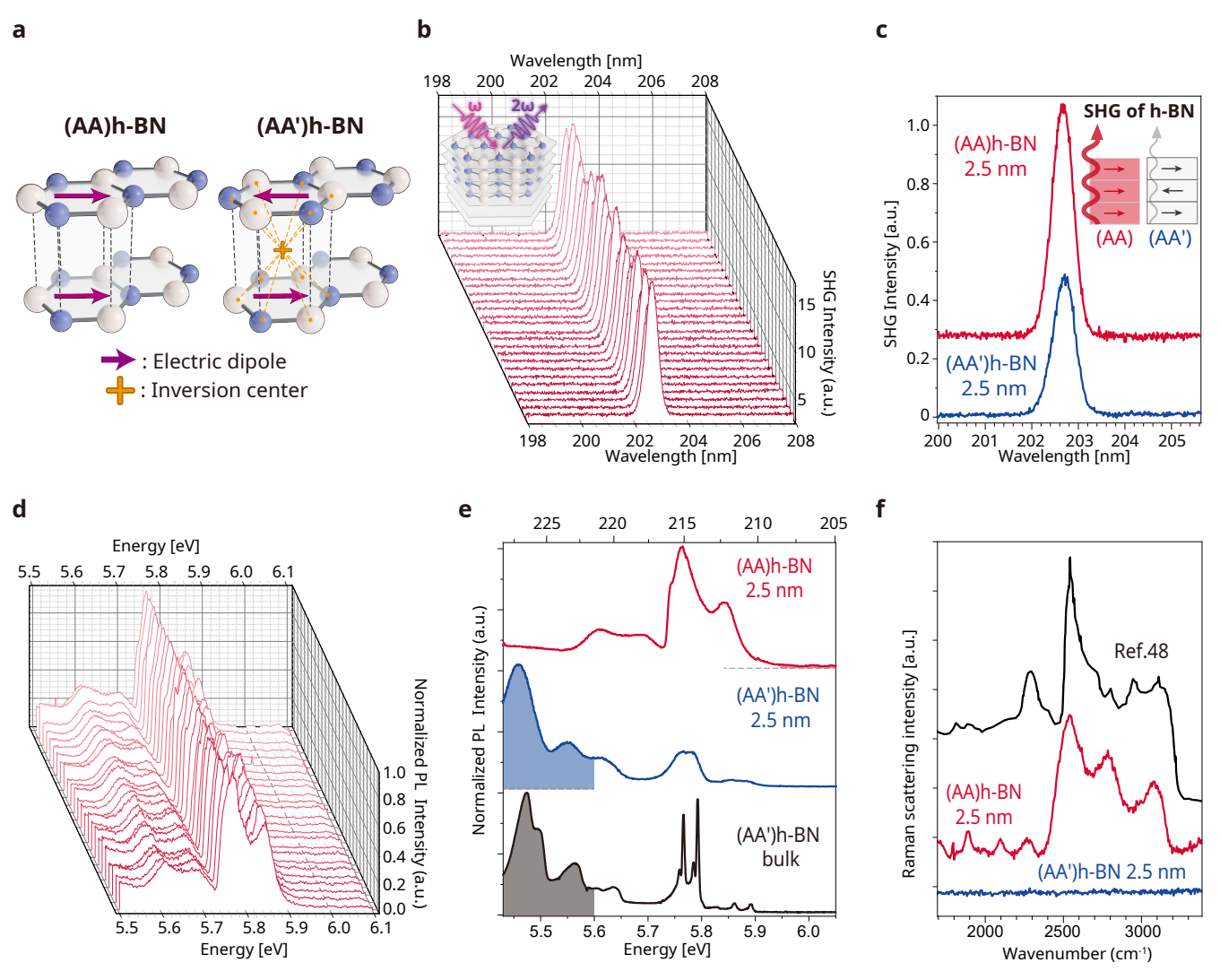
Methods-only references:

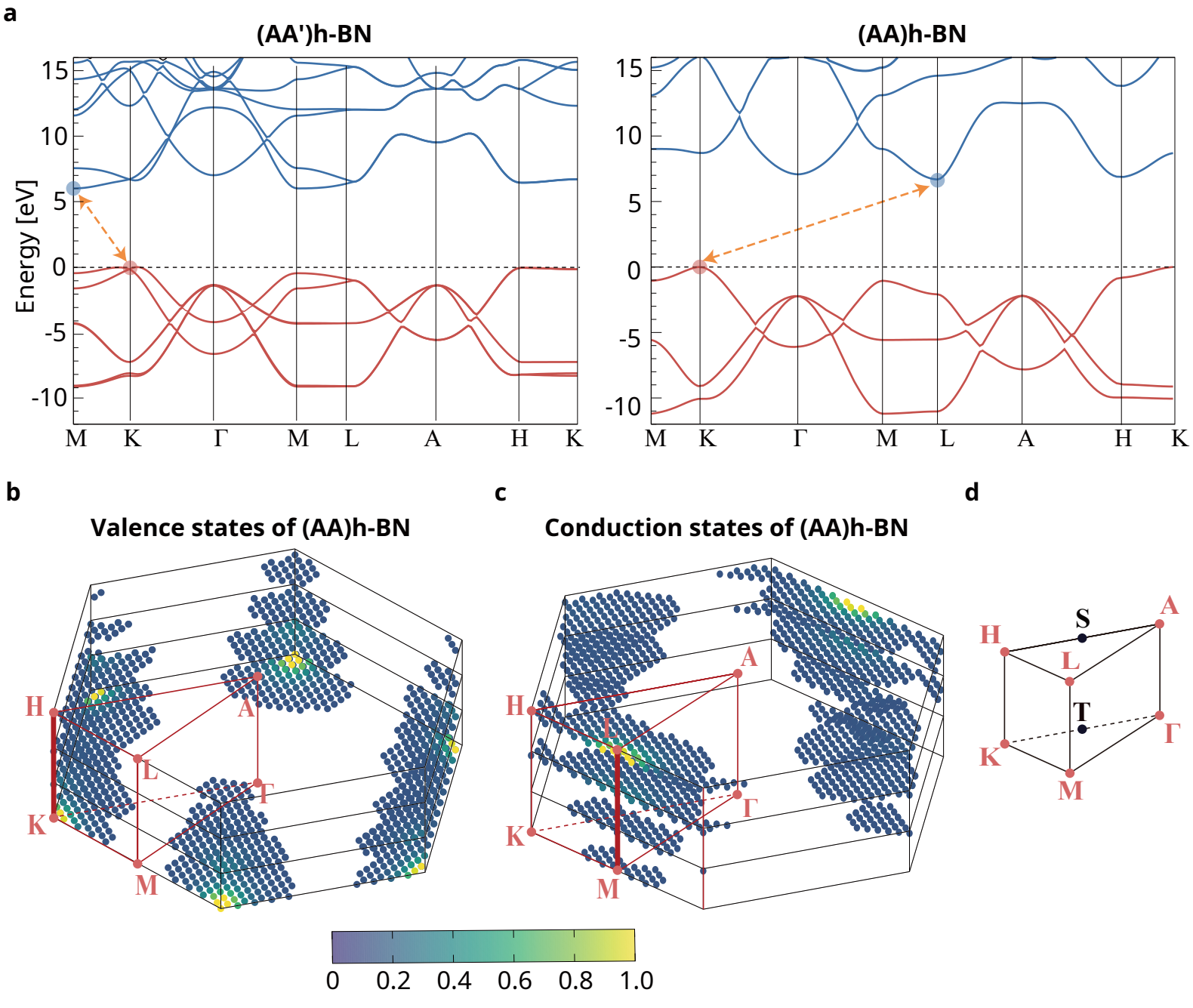
59. Giannozzi, P. *et al.* QUANTUM ESPRESSO: a modular and open-source software project for quantum simulations of materials. *J. Phys.: Condens. Matter* **21**, 395502 (2009).
60. Perdew, J. P., Burke, K. & Ernzerhof, M. Generalized Gradient Approximation Made Simple. *Phys. Rev. Lett.* **77**, 3865–3868 (1996).
61. Kresse, G. & Furthmüller, J. Efficient iterative schemes for ab initio total-energy calculations using a plane-wave basis set. *Phys. Rev. B* **54**, 11169–11186 (1996).

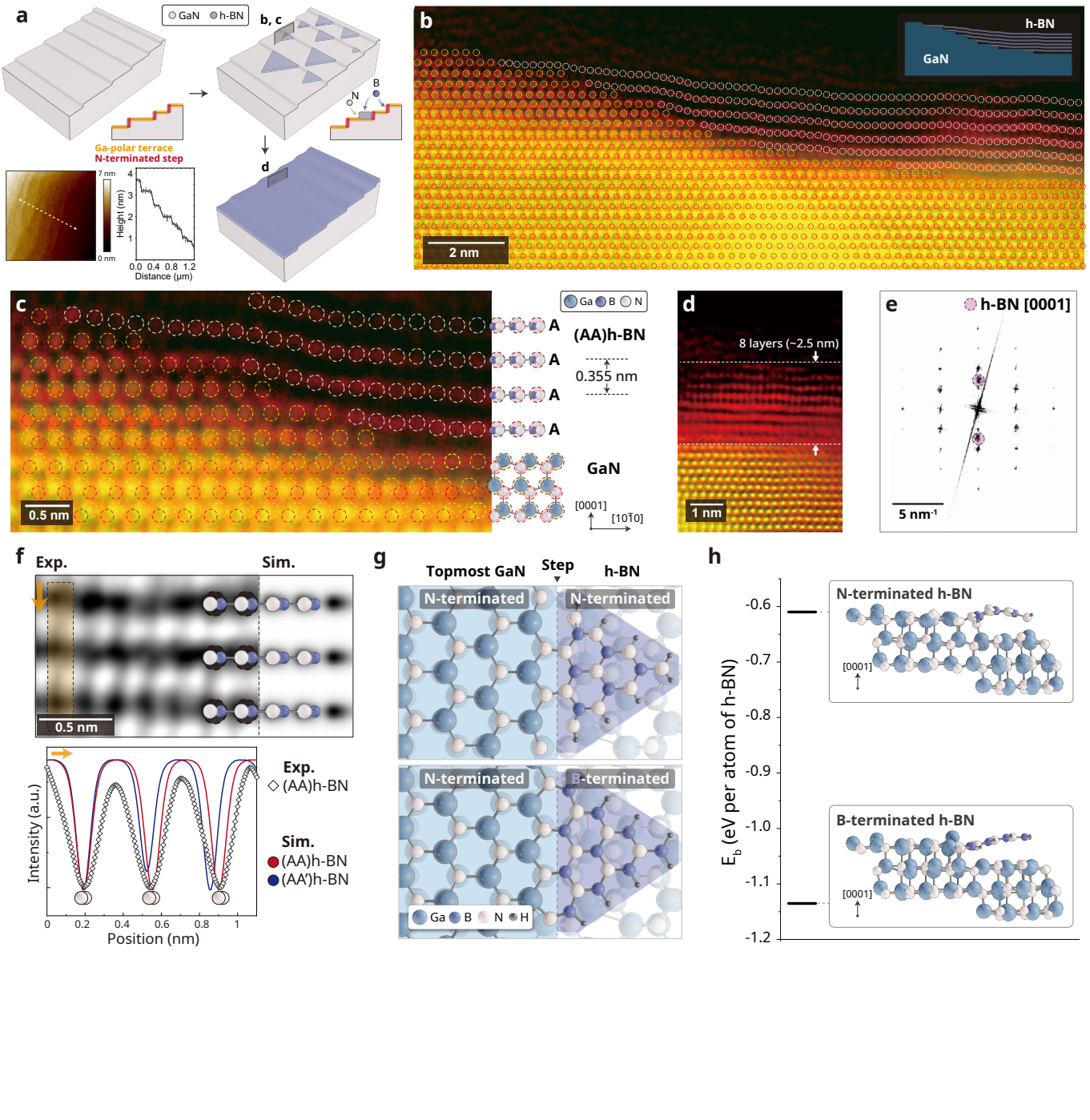
62. Kresse, G. & Furthmüller, J. Efficiency of ab-initio total energy calculations for metals and semiconductors using a plane-wave basis set. *Computational Materials Science* **6**, 15–50 (1996).
63. Grimme, S., Antony, J., Ehrlich, S. & Krieg, H. A consistent and accurate ab initio parametrization of density functional dispersion correction (DFT-D) for the 94 elements H-Pu. *J. Chem. Phys.* **132**, 154104 (2010).
64. Grimme, S., Ehrlich, S. & Goerigk, L. Effect of the damping function in dispersion corrected density functional theory. *Journal of Computational Chemistry* **32**, 1456–1465 (2011).
65. Heyd, J., Scuseria, G. E. & Ernzerhof, M. Hybrid functionals based on a screened Coulomb potential. *The Journal of Chemical Physics* **118**, 8207–8215 (2003).
66. Henck, H. *et al.* Direct observation of the band structure in bulk hexagonal boron nitride. *Phys. Rev. B* **95**, 085410 (2017).


a
TEB
Carrier gas (H2)
NH3
GaN
Sapphire
h-BN
GaN
GaN
b
2 inch.
i
ii
iii
iv
c
500 nm
d
500 nm
e
(2$\bar{1}\bar{1}$0)
(10$\bar{1}$0)
(1$\bar{1}$00)
(01$\bar{1}$0)
5nm-1
0.5 nm
f
i)
(2$\bar{1}\bar{1}$0)
(10$\bar{1}$0)
ii)
iii)
iv)
5nm-1


a
Exp.MOCVD grown (AA)h-BN
1L
2L
3L
0.5 nm
b
Exp.Exfoliated (AA')h-BN from bulk crystal
1L
3L
2L
0.5 nm
2L
3L
0.2 nm
0.2 nm
B
N
2L
3L
0.2 nm
0.2 nm
c
Sim. (AA)h-BN
Sim. (AA')h-BN
1L
2L
3L
0.5 nm
0.5 nm
d
Exp. (AA)h-BN
Exp. (AA')h-BN
Intensity (a.u.)
Position (nm)
140k
120k
100k
80k
60k
40k
20k
0
0.0
0.5
1.0
1.5
2.0
y
z
x
1L
2L
3L


a
(AA)h-BN
(AA')h-BN
: Electric dipole
: Inversion center
b
Wavelength [nm]
198 200 202 204 206 208
ω
2ω
SHG Intensity (a.u.)
15
10
5
198 200 202 204 206 208
Wavelength [nm]
c
SHG of h-BN
(AA)h-BN
2.5 nm
(AA) (AA')
(AA')h-BN
2.5 nm
SHG Intensity [a.u.]
1.0
0.8
0.6
0.4
0.2
0
200 201 202 203 204 205
Wavelength [nm]
d
Energy [eV]
5.5 5.6 5.7 5.8 5.9 6.0 6.1
Normalized PL Intensity (a.u.)
1.0
0.8
0.6
0.4
0.2
0.0
5.5 5.6 5.7 5.8 5.9 6.0 6.1
Energy [eV]
e
225 220 215 210 205
(AA)h-BN
2.5 nm
(AA')h-BN
2.5 nm
(AA')h-BN
bulk
Normalized PL Intensity (a.u.)
5.5 5.6 5.7 5.8 5.9 6.0
Energy [eV]
f
Ref.48
(AA)h-BN
2.5 nm
(AA')h-BN 2.5 nm
Raman scattering intensity [a.u.]
2000 2500 3000
Wavenumber (cm-1)


a
(AA')h-BN
(AA)h-BN
Energy [eV]
15
10
5
0
-5
-10
M K Γ M L A H K
b
Valence states of (AA)h-BN
c
Conduction states of (AA)h-BN
d
H
A
L
K
M
Γ
S
T
0 0.2 0.4 0.6 0.8 1.0


a
GaN
h-BN
b, c
d
Ga-polar terrace
N-terminated step
7 nm
0 nm
Height (nm)
Distance (μm)
b
h-BN
GaN
2 nm
c
Ga B N
A
(AA)h-BN
0.355 nm
GaN
[0001]
[10$\bar{1}$0]
0.5 nm
d
8 layers (~2.5 nm)
1 nm
e
h-BN [0001]
5 nm^{-1}
f
Exp.
Sim.
0.5 nm
Intensity (a.u.)
Position (nm)
Exp.
(AA)h-BN
Sim.
(AA)h-BN
(AA')h-BN
g
Topmost GaN
Step
h-BN
N-terminated
N-terminated
N-terminated
B-terminated
Ga B N H
h
N-terminated h-BN
B-terminated h-BN
[0001]
E_b (eV per atom of h-BN)